NANO LETTERS

Letter

pubs.acs.org/NanoLett

Anomalous Strain Relaxation in Core−Shell Nanowire Heterostructures via Simultaneous Coherent and Incoherent Growth

Ryan B. Lewis,* Lars Nicolai, Hanno Küpers, Manfred Ramsteiner, Achim Trampert, and Lutz Geelhaar

Paul-Drude-Institut für Festkörperelektronik, Hausvogteiplatz 5-7, 10117 Berlin, Germany

Supporting Information

ABSTRACT: Nanoscale substrates such as nanowires allow heterostructure design to venture well beyond the narrow lattice mismatch range restricting planar heterostructures, owing to misfit strain relaxing at the free surfaces and partitioning throughout the entire nanostructure. In this work, we uncover a novel strain relaxation process in GaAs/$In_xGa_{1-x}As$ core−shell nanowires that is a direct result of the nanofaceted nature of these nanostructures. Above a critical lattice mismatch, plastically relaxed mounds form at the edges of the nanowire sidewall facets. The relaxed mounds and a coherent shell grow simultaneously from the beginning of the deposition with higher lattice mismatches increasingly favoring incoherent mound growth. This is in stark contrast to Stranski−Krastanov growth, where above a critical thickness coherent layer growth no longer occurs. This study highlights how understanding strain relaxation in lattice mismatched nanofaceted heterostructures is essential for designing devices based on these nanostructures.

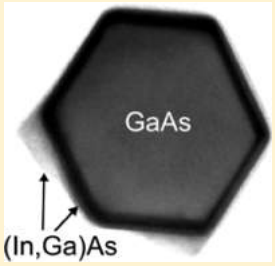

KEYWORDS: *Nanowires, core−shell, strain relaxation, X-ray diffraction, transmission electron microscopy, molecular beam epitaxy, GaAs, semiconductor*

Planar heterostructure design is highly constrained in lattice mismatch and layer thicknesses to the parameter region where misfit strain is elastically accommodated in a coherent epilayer. In other words, for a given lattice mismatch between the layer and substrate materials there exists a critical thickness, and only below this thickness will a coherently strained layer grow. Above the critical thickness, alternative strain relaxation processes take over, often resulting in severe material degradation as is the case for misfit dislocation formation.[1] However, strain relaxation can also be exploited to produce coherent low-dimensional structures such as quantum dots (QDs) by Stranski−Krastanov (SK) growth[2] and strain can favorably modify electronic properties such as band gap or carrier mobility. For these reasons, strain relaxation in planar heterostructures has been vigorously investigated.[3] Apart from planar growth, the formation of heterostructures within nanostructures such as nanowires (NWs) and nanoparticles has opened up new possibilities for heterostructure design.[4−7] These nanostructures enable the realization of coherent heterostructures well beyond the thickness and lattice mismatch ranges possible for planar growth.[8,9] This design flexibility opens the door to novel device structures based on new material combinations, which would be highly defective in planar form.

Recent investigations of strain relaxation in core−shell NW heterostructures reveal that plastic relaxation is suppressed compared to planar layers.[8,10−12] Nevertheless, for very high lattice mismatches the formation of misfit dislocations,[12−15] QDs[16−19] and shell roughening[20−22] has been observed. We note that previous investigations into the complex process of strain relaxation in core−shell NWs have focused mainly on varying NW dimensions for fixed and substantial lattice mismatches (e.g., Si/Ge or GaAs/InAs). Additionally, the nanofaceted geometry of these NW heterostructures has resulted in novel shell growth phenomena being observed, such as facet selective growth on NWs with different sidewall facets,[23,24] and surface energy effects have been exploited to realize core−shell NWs with periodically modulated shells.[25]

In this work we investigate strain relaxation in GaAs/$In_xGa_{1-x}As$ core−shell NW heterostructures with systematically varying lattice mismatch as well as core and shell dimensions, and uncover a new form of strain relaxation that is not observed in planar heterostructures. Namely, we find that above a critical lattice mismatch that depends on the core diameter, $In_xGa_{1-x}As$ shell growth proceeds partially through coherent shell growth and partially through the growth of plastically relaxed mounds. In direct contrast to SK growth, the coherent shell continues to grow after the mounds have formed and we do not observe a critical thickness for mound formation. Furthermore, the shell remains coherent with no evidence of misfit dislocations. For higher lattice mismatches, incoherent mound growth is increasingly favored over coherent shell growth. The mounds nucleate at the edges of the {110} NW sidewall facets and we explain this extraordinary strain relaxation process as a consequence of the nanofaceted nature of these heterostructures.

To investigate the influence of lattice mismatch and NW dimensions on strain relaxation, samples were grown with varying In contents and core and shell dimensions by molecular beam epitaxy (MBE) on 2 in. n-type (resistivity <0.02 Ωcm)

Received: September 1, 2016
Revised: November 17, 2016
Published: December 21, 2016

ACS Publications © 2016 American Chemical Society

DOI: 10.1021/acs.nanolett.6b03681
Nano Lett. 2017, 17, 136−142

Si(111) substrates covered by native oxide. Prior to growth, the substrates were outgassed at ~650 °C for 5−10 min in the MBE growth chamber after which the substrate temperature was reduced to 630 °C as measured by a pyrometer (calibrated to the oxide desorption temperature on GaAs substrates). Ga droplets were assembled on the substrate by depositing Ga for 30 s at 0.125 nm/s GaAs equivalent planar growth rate, followed by a 60 s flux interruption. The predeposited Ga droplets determine the NW density and increase the diameter and length uniformity of the NW distribution. Next, GaAs NW cores 3−4 μm long with ~40 nm diameter and density ~0.3 μm^{-2} were grown by Ga-assisted vapor−liquid−solid growth[26] by supplying Ga and As_2 for 50 min at 0.031 and 0.22 nm/s equivalent GaAs growth rates, respectively. Prior to shell growth, the VLS Ga droplets were consumed by exposure to As_2 at 3.0 nm/s. GaAs and $In_xGa_{1-x}As$ shells were grown at conditions that limit adatom diffusion on the NW sidewalls,[27] namely substrate temperature 390 °C and V/III flux ratios of 40−50 (total group III flux ≈0.06 nm/s). The nominal In content of the $In_xGa_{1-x}As$ shells was taken as the ratio of the In flux to the total group III flux, consistent with reports for $In_xGa_{1-x}As$ shells grown at similar conditions.[27,28] The MBE sources (2 Ga, In, and As_2) were inclined from the substrate normal by 33.5° and samples were rotated at 0.17 Hz during core and shell growth. From this geometry, NW sidewall growth rates of 0.21 times the planar growth rate are expected, consistent with the NW diameters and parasitic layer thickness observed in Figure 1. Three sample series were grown: two GaAs/$In_xGa_{1-x}As$/GaAs core−shell−shell series with nominal structures (core diameter/$In_xGa_{1-x}As$ shell thickness/outer GaAs shell thickness) 140 nm/35 nm/35 nm and 40 nm/18 nm/18 nm and a GaAs/$In_xGa_{1-x}As$ core−shell series with dimensions 140 nm/18 nm. The lattice mismatch was systematically varied by changing the In content of the shells from 20 to 100% In for the 35 nm shell series and from 20 to 60% for the two 18 nm shell series.

X-ray diffraction (XRD) measurements on as-grown core−shell NW ensembles were performed with Cu $k_{\alpha 1}$ radiation from a PANalytical X'Pert Pro Materials Research Diffractometer. To probe the NW strain in the axial direction, (111) $\omega/2\theta$ scans were carried out using both a 1 mm detector slit (divergence ~ 0.18°) and a three-bounce analyzer crystal (~12 in. divergence). Micro-Raman measurements were carried out with a Horiba/Jobin Yvon LabRAM HR Evolution system equipped with a 405 nm solid-state laser for optical excitation and a liquid nitrogen-cooled CCD for the detection of the scattered light. The spectra were recorded in backscattering geometry from single NWs dispersed on MgO(001) substrates (first-order Raman scattering forbidden by selection rules) with the incident and detected scattered light polarized along the NW axis. In order to optimize the selective enhancement of the Raman efficiency in the NW cores that occurs for excitation in resonance with the E_1 transition (~3 eV) in GaAs,[29] the experiments were carried out at low temperatures (10 K). Plan-view and cross-sectional TEM specimens were prepared by first embedding the nanowires in glue, followed by mechanical grinding and dimpling. The final thinning was performed by argon ion beam milling with an energy of 3.5−4 keV under an incident angle of 3−4° using a Gatan precision ion beam polishing system. The TEM investigation was carried out in a Jeol 2100F field-emission scanning transmission electron microscope equipped with a bright-field and dark-field detector as well as a 2k × 2k CCD camera.

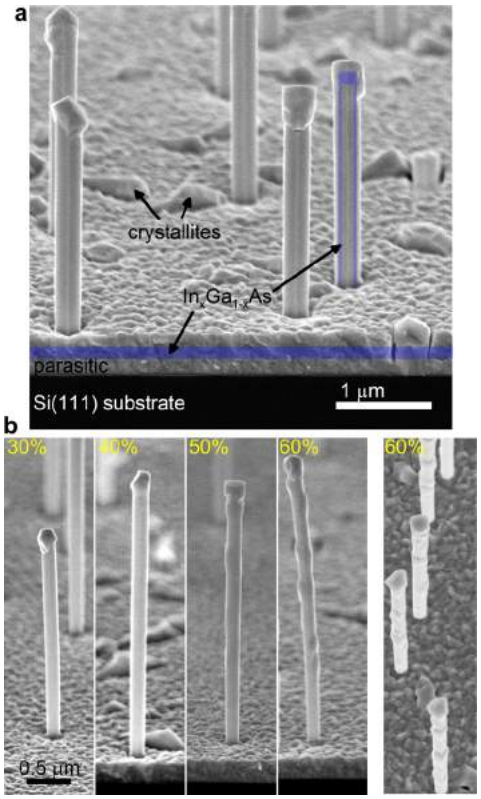

Figure 1. Scanning electron micrographs (inclined 20° from the substrate) illustrating core−shell−shell and core−shell NWs. (a) Micrograph of GaAs/$In_{0.2}Ga_{0.8}As$/GaAs core−shell−shell nanowires (nominal thicknesses 140 nm/35 nm/35 nm), a parasitic polycrystalline layer and parasitic crystallites on a Si(111) substrate. False coloring illustrates the nominal $In_{0.2}Ga_{0.8}As$ layer in a selected nanowire and the parasitic layer. (b) Images of GaAs/$In_xGa_{1-x}As$ core−shell nanowires with nominal thicknesses 140 nm/18 nm for varying In contents as indicated in the figure. The shell morphology transitions from smooth sidewalls below 40% In to increasingly rough sidewalls for higher In contents. Additional NWs with 60% In are shown in bird's eye view (inclined 70° from substrate) to further illustrate the 3D mounds on the NW sidewalls.

Figure 1a shows a scanning electron micrograph of GaAs/$In_{0.2}Ga_{0.8}As$/GaAs core−shell−shell NWs with 140 nm/35 nm/35 nm respective core diameter and shell thicknesses. The false coloring illustrates the $In_xGa_{1-x}As$ region for a selected NW and the parasitic layer. The parasitic layer is produced during the shell growth and is about five times as thick as the NW shell. X-ray diffraction measurements on a sample where the shell layers were deposited without first growing NWs reveal the parasitic layer is polycrystalline and relaxed, showing weak peaks in the $\omega/2\theta$ XRD scans only at the positions of unstrained GaAs and $In_xGa_{1-x}As$ with the nominal In content (further discussion in Supporting Information). Crystalline parasitic objects (crystallites or possibly horizontal NWs) are also visible on the substrate in Figure 1a. A series of scanning electron micrographs of GaAs/$In_xGa_{1-x}As$ core−shell NWs (140 nm/18 nm) with varying nominal In contents is depicted in Figure 1b. Shells with up to 40% In show smooth sidewall surfaces, while interestingly for higher In contents the presence of mound-like features results in increasing surface roughness.

The axial strain in the core−shell NWs was investigated by XRD on as grown NW ensembles, and by Raman spectroscopy on dispersed single NWs. Figure 2a shows $\omega/2\theta$ XRD scans

DOI: 10.1021/acs.nanolett.6b03681
Nano Lett. 2017, 17, 136−142

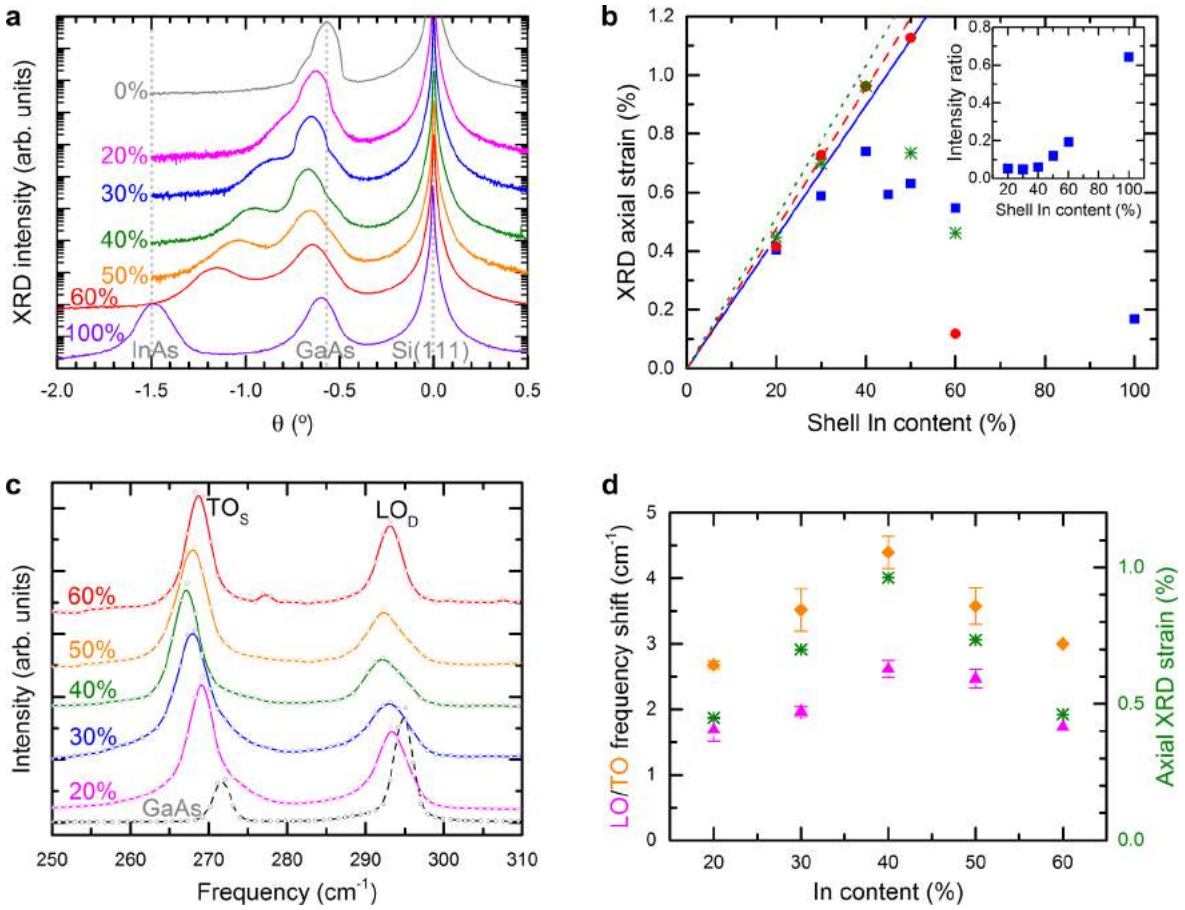

Figure 2. (a) (111) X-ray diffraction $\omega/2\theta$ scans of GaAs/$In_xGa_{1-x}As$/GaAs core−shell−shell (140 nm/35 nm/35 nm) nanowires with varying In contents. The vertical dotted lines at −1.50° and −0.57° indicate the (111) peak positions of unstrained InAs and GaAs, respectively. (b) XRD measured (points) and predicted (lines) nanowire axial strain relative to GaAs as a function of In content for GaAs/$In_xGa_{1-x}As$/GaAs nanowires with dimensions 140 nm/35 nm/35 nm (blue square, solid line), 140 nm/18 nm (green star, dotted line), and 40 nm/18 nm/18 nm (red circle, dashed line). The inset shows the In content dependence of the intensity of the relaxed $In_xGa_{1-x}As$(111) peak relative to the nanowire peak intensity for the data in (a). The largest source of uncertainty in the XRD analysis arises from the ∼10% uncertainty in the core and shell thicknesses. (c) Normalized Raman spectra of single GaAs/$In_xGa_{1-x}As$ core−shell (140 nm/18 nm) nanowires dispersed on MgO and acquired at 10 K. The low- and high-frequency peaks correspond to TO_S and LO_D scattering, respectively, in the GaAs core. The Raman spectrum of a GaAs(110) surface is shown for reference. (d) The frequency shift of the TO_S (yellow diamond) and LO_D (purple triangles) peaks and the XRD measured core strain (green star) as a function of In content. Error bars show the standard deviation when multiple NWs were measured.

across the (111) reflections from GaAs/$In_xGa_{1-x}As$/GaAs core−shell−shell NW ensembles with nominal dimensions 140 nm/35 nm/35 nm for varying In contents. A scan from bare GaAs NWs with 140 nm diameter is shown for comparison (0%). The Si(111) substrate peak (Bragg angle θ_B = 14.22°) is offset horizontally to 0° for all scans and the vertical dotted lines at −1.50° and −0.57° indicate the relaxed (111) peak positions of zincblende InAs and GaAs, respectively. The GaAs sample shows a zincblende GaAs peak with a small shoulder corresponding to wurtzite GaAs,[30] indicating the NW crystal structure is predominantly zincblende. Increasing the In content from 0 to 40% gradually shifts this NW peak to lower angles. As is discussed below, we associate this peak with the shared (111) lattice parameter of a coherent core−shell−shell NW structure and hence this trend indicates an increasing positive axial strain in the GaAs cores. Further increasing the In content from 40% to 100% has the opposite effect, reducing the strain in the GaAs core and signifying thus an increasing presence of a plastic relaxation process. The NW peak widths correspond only to the 2θ detector slit width, a consequence of an even wider distribution of tilting and bending within the NW ensemble (see Supporting Information). Each scan shows an additional peak that corresponds to the lattice parameter of unstrained $In_xGa_{1-x}As$. The absence of a partially relaxed $In_xGa_{1-x}As$ peak is startling compared to the planar situation and implies the simultaneous presence of two $In_xGa_{1-x}As$ strain states: one fully coherent with the GaAs core and outer shell, and one fully relaxed. The decreasing axial strain above 40% In coincides with an observed roughening of the NW sidewalls, similar to that shown in Figure 1b.

The inset of Figure 2b displays the unstrained $In_xGa_{1-x}As$ XRD peak intensity from Figure 2a relative to the NW peak intensity as a function of In content. Up to 40% In, the constant weak relative intensity of ∼0.05 is likely due to diffraction from the NW tips and the parasitic layer between the NWs. However, above 40% In the signal from unstrained $In_xGa_{1-x}As$ increases with increasing In content, indicating the decrease in NW axial strain coincides with an increase in the volume of unstrained $In_xGa_{1-x}As$.

For a pseudomorphic core−shell NW structure, a single shared axial lattice parameter is expected.[10,31] Neglecting variations in the elastic constants between the core and shell

DOI: 10.1021/acs.nanolett.6b03681
Nano Lett. 2017, 17, 136−142

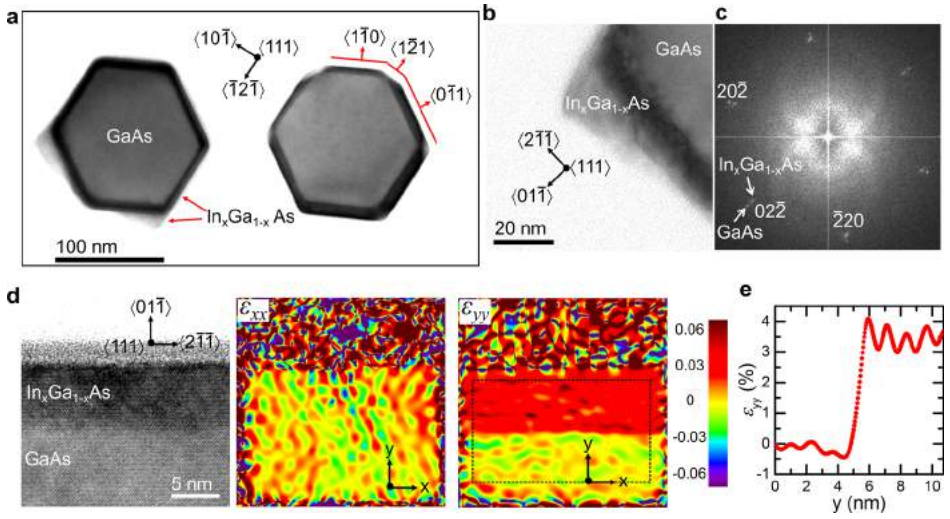

Figure 3. Bright-field plan-view scanning TEM investigation (along the ⟨111⟩ zone axis) of nominally GaAs/$In_{0.6}Ga_{0.4}As$ (140 nm/18 nm) NWs. (a) Core−shell NWs with $In_xGa_{1-x}As$ mounds and {112} facets at the edges of {110} sidewalls. (b) HR micrograph and (c) corresponding Fourier transform of an $In_xGa_{1-x}As$ mound reveal near complete strain relaxation to the GaAs core. (d) HR micrograph of the GaAs/$In_xGa_{1-x}As$ core−shell interface near the center of a {110} facet and corresponding GPA plots of in-plane (ε_{xx}) and out-of-plane (ε_{yy}) strain, illustrating the coherent core−shell interface. (e) The out-of-plane strain laterally averaged over the region defined in the ε_{yy} map is plotted as a function of distance, illustrating the abrupt core−shell interface.

materials, the resulting shared lattice parameter is according to elastic theory the average of the unstrained lattice parameters of each material in the structure, weighted by their relative cross sectional area.[10] The thus predicted axial strain (relative to unstrained zincblende GaAs) for coherent core−shell structures is plotted as a function of In content in Figure 2b for the three sample geometries assuming the nominal NW dimensions. Figure 2b also shows the axial NW strain inferred from XRD measurements for the three NW geometries. For all three series, axial strain initially increases linearly with increasing In content, in agreement with the elastic theory calculations. However, above 40% In the strain in the two 140 nm core series deviates from the calculation, decreasing gradually with further increasing In content. By comparison, the 40 nm core series deviates from the calculation only above 50% In, showing an abrupt and near complete drop in the core strain for 60% In. This difference between the sample series implies that the critical lattice mismatch for the occurrence of plastic relaxation is higher for the thinner core, which is consistent with previous reports.[8,10−12] For all three sample series, the decreasing axial NW strain coincides with the appearance of NW sidewall roughening.

To corroborate the XRD investigation, resonance Raman scattering measurements were carried out on single GaAs/$In_xGa_{1-x}As$ core−shell NWs (140 nm/18 nm) dispersed on MgO(001) substrates. Figure 2c displays single NW Raman spectra for varying In contents, where the low- and high-frequency peaks correspond to the transverse optical singlet (TO_S) and longitudinal optical doublet (LO_D) phonon modes of the GaAs core, respectively.[32] The Raman spectra are dominated by scattering from the GaAs core due to a resonance enhancement, as the 405 nm excitation is resonant with the E_1 transition of GaAs but not resonant with the $In_xGa_{1-x}As$ shell.[29] The TO_S and LO_D phonon frequencies have a linear dependence on the axial strain in the GaAs core,[32] given by the phonon deformation potentials.[32−34] The observed TO_S and LO_D frequency shifts are plotted in Figure 2d, along with the XRD measured axial strain, showing qualitative agreement between both measurements.

Transmission electron microscopy (TEM) measurements were carried out on the 60% (140 nm/18 nm) sample from Figure 1b to investigate the microstructure of the roughened NW shells. Figure 3a presents bright-field plan-view micrographs of two NWs taken along the ⟨111⟩ NW axis. Both NWs show hexagonal cores composed of {110} facets and $In_xGa_{1-x}As$ shells with a thickness of 8−12 nm, less than the nominal value of 18 nm (due to the formation of mounds on the sidewalls and possibly shadowing from neighboring NWs). We note that for $In_{0.6}Ga_{0.4}As$ growth on planar GaAs(100) the critical thickness is ∼1 nm.[35] Furthermore, in a study of similarly lattice mismatched Si/Ge core−shell NWs, Stranski−Krastanov growth with a wetting layer thickness of 1−2 nm was reported.[23] For the NW on the left of Figure 3a, two faceted mounds are visible near the corners of the sidewall facets. The location and shape of the mounds suggests they nucleated at the edges of the {110} sidewalls. In the right-hand image, {112} facets are present at some of the {110} facet corners. Measurements on other NWs from this sample show similar mound features and {112} facets. Faceted mounds on NW sidewalls have been previously observed for the Si/Ge system[20,23] as well as GaAs/GaSb and GaP/GaSb,[36] albeit not on {110} sidewall facets. For $In_xGa_{1-x}As$ shells grown on GaAs NW sidewalls, it has been shown that three-dimensional (3D) quantum dot (QD) formation readily occurs on {112} sidewalls but is suppressed on {110} sidewalls.[19] Furthermore, for InAs growth on planar GaAs(110), two-dimensional (2D) layer growth is believed to always be favored over 3D growth.[37,38] We note that InAs QD growth has been observed for both planar surfaces[39] and NW shells[16] on AlAs(110). Interestingly, the growth of (Al,Ga)As shells around GaAs NW cores has been shown to also result in {112} facets forming at the edges of the {110} NW sidewalls.[40] We propose that in our case the formation of {112} facets at the NW corners and the different relaxation processes on these surfaces, or simply the

DOI: 10.1021/acs.nanolett.6b03681
Nano Lett. 2017, 17, 136−142

edges of the {110} facets themselves, provide a pathway for strain relaxation through 3D growth of mounds.

A plan-view high-resolution (HR) micrograph of a mound at a NW corner is displayed in Figure 3b, along with a Fourier transform of the image in Figure 3c. The $In_xGa_{1-x}As$ spots in the Fourier transform exhibit negligible tetragonal distortion, indicating the $In_xGa_{1-x}As$ in the mound is nearly completely relaxed. An HR micrograph showing a GaAs/$In_xGa_{1-x}As$ core–shell interface from near the center of a {110} sidewall facet is depicted in Figure 3d along with corresponding geometric phase analysis[41] (GPA) maps for in-plane (ε_{xx}) and out-of-plane (ε_{yy}) strain relative to the GaAs core. The GPA maps demonstrate that the GaAs/$In_xGa_{1-x}As$ interface is coherent along $\langle 2\bar{1}1\rangle$. The out-of-plane GPA strain ε_{yy} is plotted as a function of distance along the direction perpendicular to the core–shell interface in Figure 3e for the rectangle defined in the ε_{yy} map. This plot reveals an extremely abrupt interface (~0.7 nm wide) and uniform strain profile throughout the thickness of the shell, indicating the In content is uniform in the observed region. The average strain value of 3.5% perpendicular to the interface seen in this plot is less than expected for an In content of 60%. By comparison, the lattice spacing in the relaxed mound in Figure 3b is ~6% larger than in the GaAs core, therefore suggesting the mound is In rich and the shell is In poor. However, other HR micrographs reveal shell strains as high as 7.5% [cf. Figure 4c]. The strain state of the mound in Figure 3b is unknown in the out of plane direction but assuming strain is completely relaxed the lattice spacing corresponds to an In content of ~80%. It is expected that In enrichment of the mounds will deplete the neighboring shell regions of In, and that the size and shape of these depleted regions will depend on how In diffuses on the surface.

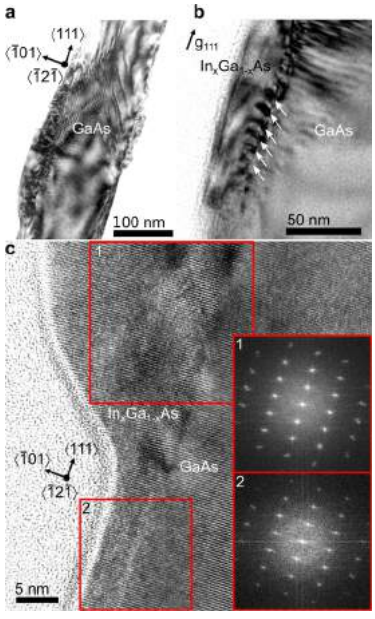

Figure 4. Cross-sectional TEM investigation of nominally GaAs/$In_{0.6}Ga_{0.4}As$ core–shell (140 nm/18 nm) NWs. (a) An overview micrograph along $\langle 11\bar{2}\rangle$ of $In_xGa_{1-x}As$ mounds and (b) a higher magnification image of a core-mound interface rotated about the $\langle 111\rangle$ axis, revealing an array of dislocations. (c) HR micrograph along $\langle 11\bar{2}\rangle$ illustrating the coherent core–shell interface and a partially relaxed $In_xGa_{1-x}As$ mound, along with Fourier transforms of two regions of the image.

A side-view TEM micrograph showing an overview of a GaAs/$In_{0.6}Ga_{0.4}As$ core–shell NW taken along the $\langle 11\bar{2}\rangle$ is presented in Figure 4a. In Figure 4b, a higher-magnification image of the mound on the left side of Figure 4a is displayed, where the NW has been rotated about its $\langle 111\rangle$ axis to incline the GaAs/$In_xGa_{1-x}As$ interface, revealing an array of dislocations near the interface. A HR micrograph showing the meeting of an $In_xGa_{1-x}As$ mound and shell is displayed in Figure 4c. No dislocations are found in the $In_xGa_{1-x}As$ shell, with the corresponding Fourier transform indicating the shell is coherently strained to the GaAs core along the NW axis. The $In_xGa_{1-x}As$ mound shows evidence of dislocations and the Fourier transform reveals predominant strain relaxation and a 1.5° tilt compared to the GaAs core. The lattice spacing of the mound and shell perpendicular to the interface are 6.5–7.5% larger than the GaAs core. However, the mound in Figure 4c has an in-plane lattice parameter of 5.5–6% larger than the GaAs core and coherent $In_xGa_{1-x}As$ shell (values are obtained based on the FFTs shown in the insets), further suggesting an enhanced In content in the mound compared to the shell. In our investigation of several NWs from this sample in both plan-view and side-view projections, no evidence for dislocations in the $In_xGa_{1-x}As$ shell away from the mounds was detected. We therefore conclude that the $In_xGa_{1-x}As$ shell is fully coherent with the GaAs core.

Considering the XRD and TEM results together, a more complete understanding of the strain relaxation process appears. The decreasing axial strain measured with XRD for higher In contents results from a thinning of the coherent $In_xGa_{1-x}As$ shell as relaxed mounds form at the corners of the NWs and consume some of the supplied material. This shell thinning was confirmed by SEM, where the NW diameter is found to decrease with increasing In content above the critical In content. Because the amount of $In_xGa_{1-x}As$ coherent to GaAs is thus smaller than assumed for the elastic strain calculations, the shared (111) lattice constant is closer to the one of GaAs. The increasing volume of relaxed mounds explains the increasing XRD intensity associated with relaxed $In_xGa_{1-x}As$. Apart from the mounds, the core–shell–shell structure remains coherent and thus no splitting of the (111) NW peak is observed.

In order to analyze how the $In_xGa_{1-x}As$ growth is divided between the coherent shell and the relaxed mounds, we calculate from the axial strain measured by XRD the actual $In_xGa_{1-x}As$ shell thickness (according to the strain model discussed above). Here we assume the nominal shell In content and nominal GaAs core and shell dimensions (i.e., only allowing the coherent $In_xGa_{1-x}As$ shell thickness to vary), and divide the resulting value by the nominal shell thickness. The corresponding results are presented for the two NW series with 140 nm core diameter but different nominal shell thickness in Figure 5 and illustrate the fraction of $In_xGa_{1-x}As$ that is devoted to the coherent shell growth. We note that the SEM of the sample with 100% In (lower inset of Figure 5) reveals a total NW thickness (between mounds) corresponding to the nominal thickness of the GaAs core and shell, supporting the very thin InAs shell value displayed in Figure 5. This InAs shell morphology resembles that of group IV core–shell NWs grown by Plateau–Rayleigh crystal growth.[25,42] Remarkably, for both series in Figure 5 the normalized $In_xGa_{1-x}As$ shell thickness shows the same dependence on In content, indicating the distribution of $In_xGa_{1-x}As$ between the shell and the mounds is independent of the amount of deposited $In_xGa_{1-x}As$. There-

DOI: 10.1021/acs.nanolett.6b03681
Nano Lett. 2017, 17, 136–142

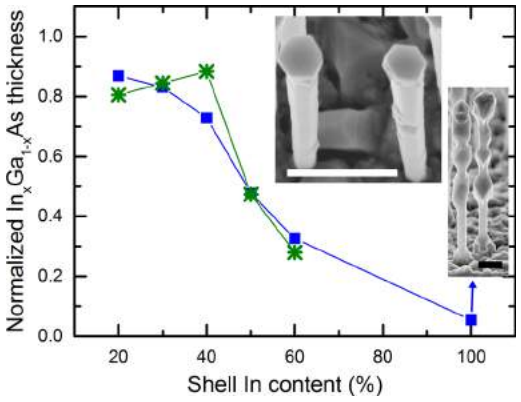

Figure 5. Coherent $In_xGa_{1-x}As$ thickness normalized to the nominal value as a function of In content as deduced from the XRD-measured axial strain. The nominal sample structures are GaAs/$In_xGa_{1-x}As$/GaAs 140 nm/35 nm/35 nm (blue square) and GaAs/$In_xGa_{1-x}As$ 140 nm/18 nm (green star), and the nominal GaAs dimensions and In contents are assumed for the calculation. The agreement between the two data sets indicates the partitioning of $In_xGa_{1-x}As$ between coherent shell and relaxed mound growth is independent of thickness, indicating both occur simultaneously. The upper inset displays an SEM image (inclined 70° from substrate) of GaAs/$In_{0.6}Ga_{0.4}As$ NWs with nominal dimensions 140 nm/5 nm, indicating the presence of $In_xGa_{1-x}As$ mounds on the NW sidewalls. A micrograph of the GaAs/InAs/GaAs NWs (inclined 20° from substrate) is shown in the lower inset. The SEM scale bars correspond to 0.5 μm.

fore, from the early stages of $In_xGa_{1-x}As$ deposition simultaneous growth of the coherent shell and relaxed mounds occurs. In fact, this conclusion was confirmed by growing a sample with 140 nm core diameter and a nominally 5 nm thick $In_{0.6}Ga_{0.4}As$ shell (thinner than the coherent shell in Figure 3). Even for this thin shell sample, mounds are visible in SEM (see upper inset to Figure 5).

The unusual relaxation mode uncovered here is fundamentally different from SK growth. In the case of SK, growth is initially 2D until a critical thickness is reached at which the formation of 3D islands becomes energetically favorable. The 3D islands release misfit strain at the cost of an increase in surface energy. After the 3D islands have formed, continued deposition increases the size and density of the islands, but growth of the wetting layer does not occur as it is energetically unfavorable. By contrast, here we observe simultaneous 2D and 3D growth, and to shell thicknesses of more than an order of magnitude greater than those reported for SK growth (on both NWs and planar substrates, as discussed above). As for SK growth, we expect strain relaxation to act as a driving force for transporting material from the coherent shell to the relaxed mounds. Therefore, the continued coherent shell growth suggests that growth kinetics play a role in limiting material collection at the mounds. As the thickness of the coherent shell increases, the shell strain decreases due to strain sharing between the core and shell and due to strain relaxation at the NW surface. This reduces the driving force for mound formation with increasing shell thickness. We note that for growth on compliant substrates as well as NW sidewalls, strain transfer from lattice mismatched islands to the NW or compliant substrate has been found to affect subsequent island nucleation.[42,43] For growth on nanofacets, the enhanced strain relaxation compared to planar growth has been predicted to suppress the nucleation of 3D islands,[44] but it has also been shown that material transfer between facets can induce early nucleation of 3D islands.[45] Finally, the extremely abrupt decrease in measured axial strain for the NW series with 40 nm core diameter [cf. Figure 2b] indicates the relaxation process depends strongly on the NW diameter. The faster relaxation in this case could be related to the shorter distance that adatoms have to diffuse to reach the facet edges. Alternatively, the smaller sidewall facets could change their orientation more easily. Nevertheless, adjusting growth conditions could provide a means for controlling the relaxation process.

We demonstrate that coherent $In_xGa_{1-x}As$ shells with up to 50% In and thicknesses exceeding 10 nm can grow around GaAs NWs. A thick $In_{0.5}Ga_{0.5}As$ layer biaxially strained to the GaAs lattice parameter is expected to have a band gap of ~0.92 eV at 300 K,[46] corresponding to an emission wavelength in excess of 1.3 μm. We therefore deduce that these structures are promising for optoelectronic devices operating at telecommunication wavelengths on the Si platform, which is in line with recent demonstrations of core−shell NW GaAs/$In_xGa_{1-x}As$ light emitting diodes[27,47] and $In_xGa_{1-x}As$/GaAs optically pumped lasers[48,49] on Si at lower In contents.

An anomalous strain relaxation process has been revealed in lattice mismatched GaAs/$In_xGa_{1-x}As$ core−shell nanowires. Above a critical In content (~40% for 140 nm core diameter), the deposited $In_xGa_{1-x}As$ grows simultaneously as a coherent shell and as plastically relaxed mounds. Mound growth is increasingly favored for increasing lattice mismatch, that is, higher In contents, consistent with strain relief being the driving force for mound growth. The simultaneous occurrence of two growth modes is a consequence of the nanofaceted nature of these nanoheterostructures, which provides alternative relaxation pathways that are not available in planar heterostructures. Such pathways can be provided by different relaxation dynamics at facet corners or on facets of different orientation within the nanostructure (such as the {110} and {112} facets observed in this case). We note that prior demonstrations of facet selective growth of Si/Ge core−shell nanowires also exploit the nanofaceted NW geometry, specifically the different surface energies and precursor decomposition rates between different facets.[23,24] Our findings are expected to have general implications for lattice mismatched nanoscale heterostructures and motivate further exploring and exploiting complex strain relaxation processes in these structures, suggesting sidewall facet optimization can play an important role in the growth of highly lattice mismatched nanowire heterostructures. Finally, this work illustrates that GaAs/$In_xGa_{1-x}As$ core−shell heterostructures show promise for optoelectronic devices with extended composition and thus wavelength range compared to planar heterostructures.

■ ASSOCIATED CONTENT

Supporting Information

The Supporting Information is available free of charge on the ACS Publications website at DOI: 10.1021/acs.nanolett.6b03681.

X-ray diffraction measurements carried out with an analyzer crystal, reciprocal space maps, and further discussion of bending and tilting within the NW ensemble (PDF)

■ AUTHOR INFORMATION

Corresponding Author

*E-mail: lewis@pdi-berlin.de.

DOI: 10.1021/acs.nanolett.6b03681
Nano Lett. 2017, 17, 136−142

ORCID

Ryan B. Lewis: 0000-0002-7216-3541

Author Contributions

R.B.L. grew the samples with help from H.K. and investigated samples by XRD. L.N. and A.T. analyzed samples by TEM and M.R. by Raman spectroscopy. R.B.L. and L.G. conceived the study with contributions by A.T. R.B.L. along with L.G. composed the manuscript and all authors discussed the results and commented on the manuscript.

Notes

The authors declare no competing financial interest.

■ ACKNOWLEDGMENTS

This work was partially funded by Deutsche Forschungsgemeinschaft under Grant Ge2224/2. R.B.L. acknowledges additional funding from the Alexander von Humboldt Foundation. The authors are grateful to A.-K. Bluhm for her SEM work and M. Höricke and C. Stemmler for MBE maintenance. The authors would like to thank U. Pietsch for discussions and S. Fölsch for a critical reading of the manuscript.

■ REFERENCES

(1) Matthews, J. W.; Blakeslee, A. E. *J. Cryst. Growth* **1974**, *27*, 118−125.
(2) Stangl, J.; Holý, V.; Bauer, G. *Rev. Mod. Phys.* **2004**, *76* (3), 725−783.
(3) Jain, S. C.; Willander, M.; Maes, H. *Semicond. Sci. Technol.* **1996**, *11* (6), 641−671.
(4) Lauhon, L. J.; Gudiksen, M. S.; Wang, D.; Lieber, C. M. *Nature* **2002**, *420* (6911), 57−61.
(5) Björk, M. T.; Ohlsson, B. J.; Sass, T.; Persson, a. I.; Thelander, C.; Magnusson, M. H.; Deppert, K.; Wallenberg, L. R.; Samuelson, L. *Nano Lett.* **2002**, *2* (2), 87−89.
(6) Gudiksen, M. S.; Lauhon, L. J.; Wang, J.; Smith, D. C.; Lieber, C. M. *Nature* **2002**, *415* (6872), 617−620.
(7) Cao, Y. W.; Banin, U. *J. Am. Chem. Soc.* **2000**, *122* (40), 9692−9702.
(8) Kavanagh, K. L. *Semicond. Sci. Technol.* **2010**, *25* (2), 024006.
(9) Gutkin, M. Y.; Kolesnikova, A. L.; Krasnitsky, S. A.; Romanov, A. E. *Phys. Solid State* **2014**, *56* (4), 723−730.
(10) Liang, Y.; Nix, W. D.; Griffin, P. B.; Plummer, J. D. *J. Appl. Phys.* **2005**, *97* (4), 043519.
(11) Trammell, T. E.; Zhang, X.; Li, Y.; Chen, L.-Q.; Dickey, E. C. *J. Cryst. Growth* **2008**, *310* (12), 3084−3092.
(12) Salehzadeh, O.; Kavanagh, K. L.; Watkins, S. P. *J. Appl. Phys.* **2013**, *114* (5), 054301.
(13) Dayeh, S. A.; Tang, W.; Boioli, F.; Kavanagh, K. L.; Zheng, H.; Wang, J.; Mack, N. H.; Swadener, G.; Huang, J. Y.; Miglio, L.; Tu, K. N.; Picraux, S. T. *Nano Lett.* **2013**, *13* (5), 1869−1876.
(14) Kavanagh, K. L.; Salfi, J.; Savelyev, I.; Blumin, M.; Ruda, H. E. *Appl. Phys. Lett.* **2011**, *98* (15), 152103.
(15) Kavanagh, K. L.; Saveliev, I.; Blumin, M.; Swadener, G.; Ruda, H. E. *J. Appl. Phys.* **2012**, *111* (4), 044301.
(16) Uccelli, E.; Arbiol, J.; Morante, J. R.; Fontcuberta i Morral, A. *ACS Nano* **2010**, *4* (10), 5985−5993.
(17) Yan, X.; Zhang, X.; Ren, X.; Lv, X.; Li, J.; Wang, Q.; Cai, S.; Huang, Y. *Nano Lett.* **2012**, *12* (4), 1851−1856.
(18) Guo, J.; Huang, H.; Zhang, J.; Li, X.; Huang, Y.; Ren, X.; Ji, Z.; Liu, M. *J. Appl. Phys.* **2013**, *113* (11), 114301.
(19) Yan, X.; Zhang, X.; Ren, X.; Li, J.; Lv, X.; Wang, Q.; Huang, Y. *Appl. Phys. Lett.* **2012**, *101*, 023106.
(20) Goldthorpe, I. A.; Marshall, A. F.; McIntyre, P. C. *Nano Lett.* **2008**, *8* (11), 4081−4086.
(21) Schmidt, V.; McIntyre, P.; Gösele, U. *Phys. Rev. B: Condens. Matter Mater. Phys.* **2008**, *77* (23), 235302.
(22) Goldthorpe, I. a.; Marshall, A. F.; McIntyre, P. C. *Nano Lett.* **2009**, *9* (11), 3715−3719.
(23) Pan, L.; Lew, K. K.; Redwing, J. M.; Dickey, E. C. *Nano Lett.* **2005**, *5* (6), 1081−1085.
(24) Kempa, T. J.; Kim, S. K.; Day, R. W.; Park, H. G.; Nocera, D. G.; Lieber, C. M. *J. Am. Chem. Soc.* **2013**, *135* (49), 18354−18357.
(25) Day, R. W.; Mankin, M. N.; Gao, R.; No, Y.-S.; Kim, S.-K.; Bell, D. C.; Park, H.-G.; Lieber, C. M. *Nat. Nanotechnol.* **2015**, *10* (4), 345−352.
(26) Morral, A. F. I. *IEEE J. Sel. Top. Quantum Electron.* **2011**, *17* (4), 819−828.
(27) Dimakis, E.; Jahn, U.; Ramsteiner, M.; Tahraoui, A.; Grandal, J.; Kong, X.; Marquardt, O.; Trampert, A.; Riechert, H.; Geelhaar, L. *Nano Lett.* **2014**, *14* (5), 2604−2609.
(28) Grandal, J.; Wu, M.; Kong, X.; Hanke, M.; Dimakis, E.; Geelhaar, L.; Riechert, H.; Trampert, A. *Appl. Phys. Lett.* **2014**, *105* (12), 121602.
(29) Trommer, R.; Cardona, M. *Phys. Rev. B: Condens. Matter Mater. Phys.* **1978**, *17* (4), 1865−1876.
(30) Köhl, M.; Schroth, P.; Minkevich, A. a.; Hornung, J.-W.; Dimakis, E.; Somaschini, C.; Geelhaar, L.; Aschenbrenner, T.; Lazarev, S.; Grigoriev, D.; Pietsch, U.; Baumbach, T. *J. Synchrotron Radiat.* **2015**, *22* (1), 67−75.
(31) Grönqvist, J.; Søndergaard, N.; Boxberg, F.; Guhr, T.; Åberg, S.; Xu, H. Q. *J. Appl. Phys.* **2009**, *106* (5), 053508.
(32) Signorello, G.; Karg, S.; Björk, M. T.; Gotsmann, B.; Riel, H. *Nano Lett.* **2013**, *13* (3), 917−924.
(33) Cerdeira, F.; Buchenauer, C. J.; Pollak, F. H.; Cardona, M. *Phys. Rev. B* **1972**, *5* (2), 580−593.
(34) Wickboldt, P.; Anastassakis, E.; Sauer, R.; Cardona, M. *Phys. Rev. B: Condens. Matter Mater. Phys.* **1987**, *35* (3), 1362−1368.
(35) Pristovsek, M.; Kremzow, R.; Kneissl, M. *Jpn. J. Appl. Phys.* **2013**, *52*, 041201.
(36) Salehzadeh, O.; Kavanagh, K. L.; Watkins, S. P. *J. Appl. Phys.* **2013**, *113* (13), 134309.
(37) Joyce, B. A.; Sudijono, J. L.; Belk, J. G.; Yamaguchi, H.; Zhang, X. M.; Dobbs, H. T.; Zangwill, A.; Vvedensky, D. D.; Jones, T. S. *Jpn. J. Appl. Phys.* **1997**, *36* (6), 4111−4117.
(38) Zhang, X.; Pashley, D. W. *J. Mater. Sci.: Mater. Electron.* **1996**, *7* (5), 361−367.
(39) Wasserman, D.; Lyon, S. A.; Hadjipanayi, M.; Maciel, A.; Ryan, J. F. *Appl. Phys. Lett.* **2003**, *83* (24), 5050−5052.
(40) Heiss, M.; Fontana, Y.; Gustafsson, A.; Wüst, G.; Magen, C.; O'Regan, D. D.; Luo, J. W.; Ketterer, B.; Conesa-Boj, S.; Kuhlmann, A. V.; Houel, J.; Russo-Averchi, E.; Morante, J. R.; Cantoni, M.; Marzari, N.; Arbiol, J.; Zunger, A.; Warburton, R. J.; Fontcuberta i Morral, A. *Nat. Mater.* **2013**, *12* (5), 439−444.
(41) Hÿtch, M. J.; Snoeck, E.; Kilaas, R. *Ultramicroscopy* **1998**, *74* (3), 131−146.
(42) Day, R. W.; Mankin, M. N.; Lieber, C. M. *Nano Lett.* **2016**, *16* (4), 2830−2836.
(43) Deneke, C.; Malachias, A.; Rastelli, A.; Merces, L.; Huang, M.; Cavallo, F.; Schmidt, O. G.; Lagally, M. G. *ACS Nano* **2012**, *6* (11), 10287−10295.
(44) Glas, F.; Daudin, B. *Phys. Rev. B: Condens. Matter Mater. Phys.* **2012**, *86* (17), 1−8.
(45) Konkar, A.; Madhukar, A.; Chen, P. *Appl. Phys. Lett.* **1998**, *72* (2), 220−222.
(46) Ji, G.; Huang, D.; Reddy, U. K.; Henderson, T. S.; Houdré, R.; Morkoç, H. *J. Appl. Phys.* **1987**, *62* (8), 3366−3373.
(47) Chuang, L. C.; Sedgwick, F. G.; Chen, R.; Ko, W. S.; Moewe, M.; Ng, K. W.; Tran, T.-T. D.; Chang-Hasnain, C. *Nano Lett.* **2011**, *11* (2), 385−390.
(48) Chen, R.; Tran, T.-T. D.; Ng, K. W.; Ko, W. S.; Chuang, L. C.; Sedgwick, F. G.; Chang-Hasnain, C. *Nat. Photonics* **2011**, *5* (3), 170−175.
(49) Lu, F.; Tran, T.-T. D.; Ko, W. S.; Ng, K. W.; Chen, R.; Chang-Hasnain, C. *Opt. Express* **2012**, *20* (11), 12171−12176.

DOI: 10.1021/acs.nanolett.6b03681
Nano Lett. 2017, 17, 136−142